

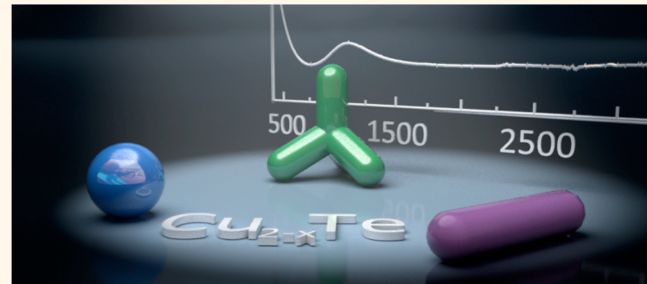
Shedding Light on Vacancy-Doped Copper Chalcogenides: Shape-Controlled Synthesis, Optical Properties, and Modeling of Copper Telluride Nanocrystals with Near-Infrared Plasmon Resonances

Ilka Kriegel,^{†,*} Jessica Rodríguez-Fernández,^{†,*} Andreas Wisnet,[‡] Hui Zhang,[§] Christian Waurisch,[†] Alexander Eychmüller,[†] Aliaksei Dubavik,^{†,‡} Alexander O. Govorov,[§] and Jochen Feldmann[†]

[†]Photonics and Optoelectronics Group, Department of Physics and CeNS, Ludwig-Maximilians-Universität München, Munich, Germany, [‡]Department of Chemistry and CeNS, Ludwig-Maximilians-Universität München, Munich, Germany, [§]Department of Physics and Astronomy, Ohio University, Athens, Ohio 45701, United States, and

[†]Department of Physical Chemistry, Technische Universität Dresden, Dresden, Germany

ABSTRACT Size- and shape-controlled synthesis of copper chalcogenide nanocrystals (NCs) is of paramount importance for a careful engineering and understanding of their optoelectronic properties and, thus, for their exploitation in energy- and plasmonic-related applications. From the copper chalcogenide family copper telluride NCs have remained fairly unexplored as a result of a poor size-, shape-, and monodispersity control that is achieved *via* one-step syntheses approaches. Here we show that copper telluride (namely Cu_{2-x}Te) NCs with well-defined morphologies (spheres, rods, tetrapods) can be prepared *via* cation exchange of preformed CdTe NCs while retaining their original shape. The resulting copper telluride NCs are characterized by pronounced plasmon bands in the near-infrared (NIR), in analogy to other copper-deficient chalcogenides (Cu_{2-x}S , Cu_{2-x}Se). We demonstrate that the extinction spectra of the as-prepared NCs are in agreement with theoretical calculations based on the discrete dipole approximation and an empirical dielectric function for Cu_{2-x}Te . Additionally we show that the Drude model does not appropriately describe the complete set of Cu_{2-x}Te NCs with different shapes. In particular, the low-intensity longitudinal plasmon bands for nanorods and tetrapods are better described by a modified Drude model with an increased damping in the long-wavelength interval. Importantly, a Lorentz model of localized quantum oscillators describes reasonably well all three morphologies, suggesting that holes in the valence band of Cu_{2-x}Te cannot be described as fully free particles and that the effects of localization of holes are important. A similar behavior for Cu_{2-x}S and Cu_{2-x}Se NCs suggests that the effect of localization of holes can be a common property for the whole class of copper chalcogenide NCs. Taken altogether, our results represent a simple route toward copper telluride nanocrystals with well-defined shapes and optical properties and extend the understanding on vacancy-doped copper chalcogenide NCs with NIR optical resonances.



KEYWORDS: copper chalcogenide nanocrystals · copper telluride nanocrystals · doped semiconductor nanocrystals · plasmon resonance · optical properties · discrete dipole approximation · Drude model · vacancy-doping

In recent years, vacancy-doped semiconductor NCs such as copper chalcogenides have gained increasing interest due to their ability to hold tunable localized surface plasmon resonances (LSPRs).^{1–12} Vacancies in the structure lead to an increased charge carrier density that, when collectively excited by electromagnetic radiation, give rise to an intense near-infrared

(NIR) extinction band, recently assigned to an LSPR.^{2,13} In the entire family of copper chalcogenide NCs, namely, copper sulfides (Cu_{2-x}S), selenides (Cu_{2-x}Se), and tellurides (Cu_{2-x}Te), the possibility to control the charge carrier density by manipulation of the copper vacancies in the structure leads to an additional means of tunability of the plasmon resonance, which is an advantage

* Address correspondence to ilka.kriegel@physik.uni-muenchen.de, jessica.rodriguez@lmu.de.

Received for review February 21, 2013 and accepted April 9, 2013.

Published online April 09, 2013
10.1021/nn400894d

© 2013 American Chemical Society

over noble metal nanoparticles.^{2,4,8} While the tunability of the carrier density represents a new pathway for LSPR tuning, NC morphology is expected to play a significant role in the LSPR frequency as well. From the copper chalcogenide family, recent works have reported on the preparation of Cu_{2-x}S and Cu_{2-x}Se NCs with well-defined sizes and morphologies,¹⁴ such as spheres,^{13,15–20} nanorods,^{3,21} and platelets.^{21–23} An exact evaluation of the NIR properties has mainly focused on monodisperse spherical particles,^{4,9} while anisotropic shapes have been only scarcely examined.^{3,24} Recently the plasmonic properties of Cu_{2-x}S nanodisks have been investigated.^{5,6} Two distinct bands in the NIR have been emphasized to represent the excitation of dipolar modes in- (lower energy mode) and out-of- (higher energy mode) the nanodisk's plane.^{5,6} Most of the theoretical considerations in the above-mentioned works were based on the application of the Drude model (*i.e.*, assuming a free carrier metal-like behavior for copper chalcogenide NCs) to the particular NC morphology under investigation.^{2,4–6,9,13} However, in optical modeling it is important that with a given model dielectric function the optical properties of NCs of varying shapes can be accounted for.

In contrast to their sulfide and selenide counterparts, the shape-controlled synthesis and optical characterization of Cu_{2-x}Te NCs still remain fairly unexplored due to a poor control over NC size, shape, monodispersity, composition, and stability obtained *via* one-step syntheses approaches.^{25–28} On a different front, the insertion and exchange of cations in ionic NCs has become a powerful tool to achieve chemical transformations and tune materials properties.²⁹ Ionic NCs can replace their cationic sublattice with a different metal ion while preserving their size, shape, and anionic framework, but with a concomitant modification of their crystal structure, composition, and optoelectronic properties.^{30–37} In this work we take advantage of shape control in ion exchange reactions to overcome the poor control attained to date on copper telluride NC synthesis and to gain access to the evaluation of their shape-dependent optical properties in the NIR. Specifically, in the first part of this article we will show how Cu_{2-x}Te NCs of precise shapes (spheres, rods, and tetrapods) can be prepared from preformed CdTe NCs through ion exchange with Cu^+ . In the second part we will focus on the investigation of the shape-dependent plasmonic properties of vacancy-doped Cu_{2-x}Te NCs through a direct comparison with theoretical modeling based on the discrete dipole approximation (DDA) method. By using a purely empirical dielectric function and phenomenological ones (Drude, Drude damped, and Lorentz models) to account for the extinction spectra of the differently shaped Cu_{2-x}Te NCs, we gain insights into the NIR optical resonances of copper chalcogenides.

RESULTS AND DISCUSSION

Our approach for the shape-controlled synthesis of copper telluride NCs relies on the utilization of CdTe nanocrystals with well-defined morphologies (namely, spheres, nanorods, and tetrapods) as "sacrificial templates" for cation exchange reactions (see sketch in Figure 1a, top panel).^{31–37} In all cases the starting CdTe NCs were synthesized through standard procedures, as thoroughly described in the Experimental Section. To perform the exchange of Cd^{2+} by Cu^+ ions in the as-prepared CdTe NCs, a 4 mg/mL Cu^+ stock was prepared by dissolving $[\text{Cu}(\text{CH}_3\text{CN})_4]\text{PF}_6$ in anhydrous methanol in a N_2 -filled glovebox. Ion exchange was performed by injecting under vigorous stirring 60 μL of the CdTe stock solution into a mixture of Cu^+ stock solution in methanol and toluene containing an excess of oleylamine. In order to ensure a complete ion exchange, the total amount of Cu^+ ions added was set to a 10 \times stoichiometric excess with respect to Cd^{2+} (as determined from ref 38; see Experimental Section for details). The ion exchange process is schematically depicted in Figure 1a.

An immediate color change from dark brown to golden upon Cu^+ addition indicated that the ion exchange occurred immediately. The HRTEM micrograph in Figure 1b representatively illustrates the crystallinity of the obtained Cu_{2-x}Te NCs (nanorods in this case). X-ray diffraction (XRD, Figure 1c), energy dispersive X-ray analysis (EDX, Figure 1d), and electron diffraction (ED, Figure 1e and f) of the NCs before (CdTe) and after (Cu_{2-x}Te) ion exchange confirm the exchange of Cd^{2+} by Cu^+ ions. The CdTe nanorods have a cubic zincblende structure (Figure 1c, orange curve) with the main diffraction peaks at 23.78, 39.33, 46.48, and 62.47 2θ angle, corresponding to the lattice planes 111, 220, 311, and 331, respectively. The stick reference powder XRD pattern of bulk CdTe (JCPDS 85-237) is shown in Figure 1c (orange bars). The first three main diffraction rings are also observed in the ED micrograph in Figure 1e and are indexed to the 111, 220, and 311 lattice planes. However, the crystal structure of the ion-exchanged Cu_{2-x}Te nanorods can be indexed to hexagonal weissite crystal structure (Figure 1c, dark red curve). Dark red bars in the same figure indicate the reference powder pattern of bulk Cu_{2-x}Te with weissite crystal structure (JCPDS 15-565). The first main peaks can be indexed to the 200, 023, 220, 029, and 226 lattice planes of bulk weissite Cu_{2-x}Te . The electron diffraction pattern of the ion-exchanged Cu_{2-x}Te nanorods in Figure 1f further confirms the weissite crystal structure. EDX measurements on a single Cu_{2-x}Te nanorod (Figure 1d) support that no Cd is present after ion exchange, thus confirming that our CdTe nanorods undergo a complete ion exchange into Cu_{2-x}Te under our experimental conditions.

In order to investigate the shape-dependent optical properties of Cu_{2-x}Te NCs, we performed copper

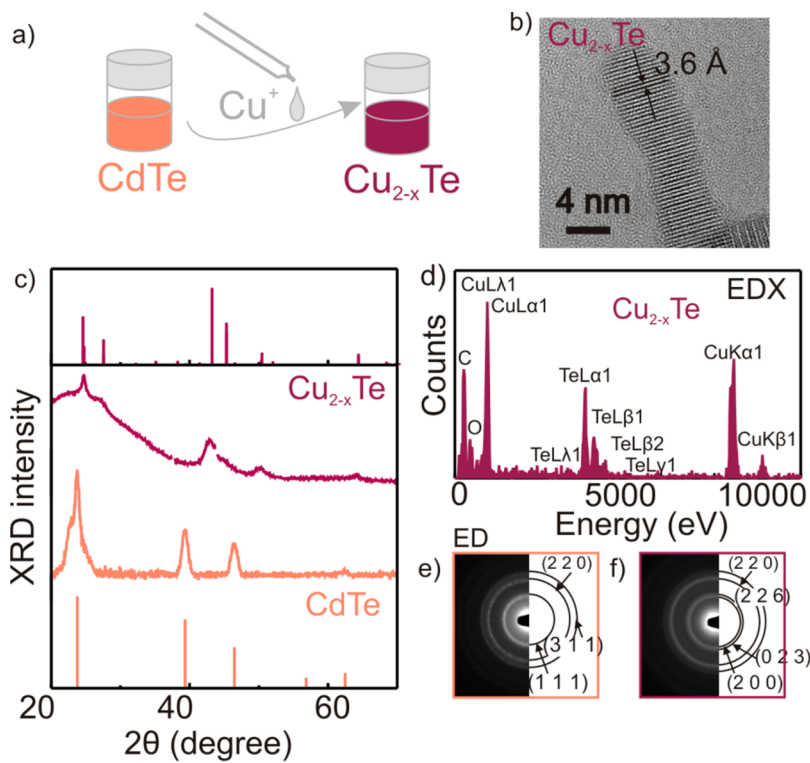


Figure 1. (a) Schematic depiction of the ion exchange process from CdTe to Cu_{2-x}Te NCs. (b) HRTEM image of a Cu_{2-x}Te NC showing its crystallinity. (c) XRD patterns of CdTe NCs (orange curves) and ion exchanged Cu_{2-x}Te NCs (dark red curves). (d) EDX spectrum of a single, ion-exchanged Cu_{2-x}Te NC. (e and f) ED pattern of CdTe and Cu_{2-x}Te NCs, respectively.

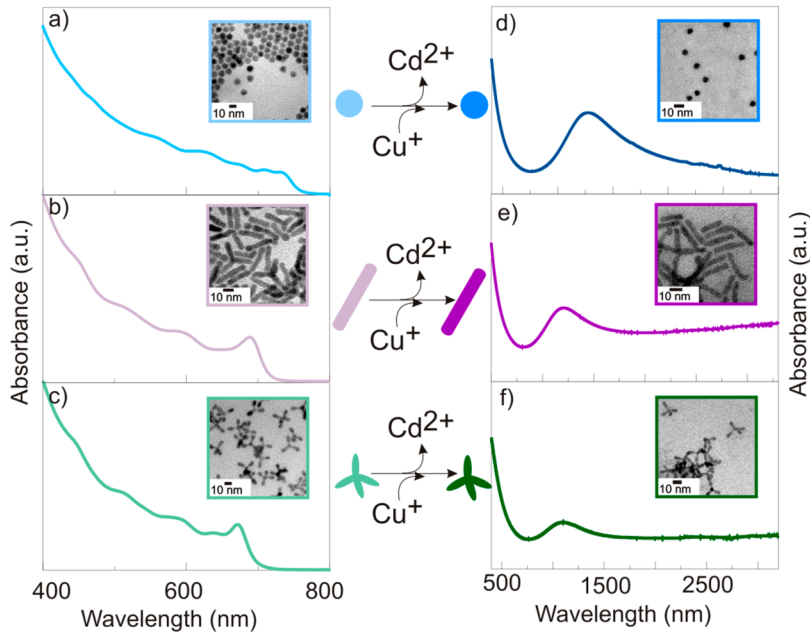


Figure 2. (a–c) Extinction spectra of CdTe NCs of varying shapes together with representative TEM images: (a) spheres, (b) rods, and (c) tetrapods. (d–f) Extinction spectra of Cu_{2-x}Te NCs of varying shapes produced via ion exchange from CdTe together with representative TEM images: (d) spheres, (e) rods, and (f) tetrapods. Center: Schematic representation of the ion exchange process.

exchange reactions according to the above-mentioned approach by using CdTe NCs of various shapes as “sacrificial templates”. These were CdTe spheres of ~9 nm diameter (Figure 2a, inset), nanorods of ~5 nm

in width and 21 nm in length (Figure 2b, inset), and tetrapods of arm length ~12 nm and arm width ~5 nm (Figure 2c, inset). The respective histograms are provided in Figures S1, S2, and S3 in the Supporting

Information. Their corresponding extinction spectra are depicted in Figure 2a–c. All spectra are characterized by pronounced peaks ascribed to excitonic transitions (see representative photoluminescence spectrum of CdTe nanorods in Figure S4, Supporting Information) since the dimensions of our CdTe NCs, *i.e.*, the diameter of the sphere and the width of the rods and tetrapods, lie within the size of the exciton bohr radius of bulk CdTe, \sim 7.3 nm.³⁹ Upon addition of a Cu⁺ excess, Cu_{2-x}Te spheres, rods, and tetrapods are obtained (see TEM images as insets in Figure 2d–f), as confirmed by XRD analysis on each shape (Figure S5 in the Supporting Information). Figure 2d–f contains the corresponding extinction spectra of the ion-exchanged Cu_{2-x}Te NCs. Please note the changed wavelength scale in the Cu_{2-x}Te NCs spectra with respect to the initial CdTe NCs spectra. After exchange the excitonic features characterizing the extinction spectra of CdTe NCs are replaced by a rather broad spectrum showing a steep extinction in the blue and a pronounced band in the NIR. In copper chalcogenides the region below \sim 700 nm is attributed to interband transitions, while the extinction band in the NIR has been ascribed to plasmon resonances due to free carriers in the NCs.^{2,4,7–9,13} After ion exchange no PL is detected, as expected for copper chalcogenide NCs showing a pronounced plasmon resonance (Figure S4 in the Supporting Information).⁸ The plasmon resonance for the spheres (Figure 2d) is located at \sim 1074 nm, with the extinction approaching zero in the NIR. In contrast, the spectra of the Cu_{2-x}Te nanorods and tetrapods, with plasmon resonances peaking at \sim 1069 and \sim 1103 nm, respectively (Figure 2e and f), show an additional broad extinction that slightly increases in intensity toward the red end of the spectrum, up to 3300 nm (our instrumental limit). Notably, FTIR measurements on the Cu_{2-x}Te nanorods (Figure S6 in the Supporting Information) show that there is no plasmon resonance mode in the mid-IR, in contrast to other doped semiconductor NCs, as recently reported by Rowe *et al.*⁴⁰ Further, higher aspect ratio (AR) Cu_{2-x}Te nanorods with dimensions of 5.5 nm in width and 48 nm in length (*i.e.*, AR = 9.6) show a very similar extinction spectrum (see Figure S7 in the Supporting Information) to that of nanorods with a lower AR (4.1, shown in Figure 2e). Despite the significant difference in the ARs, the spectrum is similarly characterized by a single plasmon resonance at *ca.* 1026 nm and a broad extinction up to 3300 nm.

To gain further insights on the effect of NC morphology on the plasmonic properties, in the following we directly compare the experimental extinction spectra of the Cu_{2-x}Te spheres, rods, and tetrapods with model calculations performed with the discrete dipole approximation. For an easier comparison with the calculations, the experimental extinction spectra of the Cu_{2-x}Te NCs are displayed in Figure 3 together with

the corresponding TEM images for each shape (top panel). The calculated extinction spectra for a single Cu_{2-x}Te sphere (9 nm diameter), rod (21 \times 5 nm length \times width, 2 nm tip radius, see Figure S8 in the Supporting Information), and tetrapod (12 \times 5 nm arm length \times width) are summarized in Figure 3 (I), (II), and (III), along with the corresponding input morphologies displayed as insets in Figure 3 (I). The extinction spectra represented in Figure 3 (I) were calculated by using an averaged empirical dielectric function from Farag *et al.*,⁴¹ determined from transmission (T) and reflectivity (R) measurements of thin Cu_{2-x}Te films of varying thicknesses (see Figure S9 in the Supporting Information and further discussion below). The calculated spectra represented in Figure 3a(I), b(I) (thick solid curve, averaged over all directions of light incidence) and c(I) for the three shapes show a good qualitative agreement with the experimental ones, representing the steep extinction in the blue due to interband transitions, as well as the NIR plasmon bands. [Note that the shoulder centered at *ca.* 740 nm in the calculated spectrum of the sphere (Figure 3a(I)) is due to an artifact from the empirical input data at that wavelength and is not visible in the nanorod and tetrapod spectra due to their higher extinction cross section at 740 nm.] Nevertheless, a mismatch between the calculated and experimental spectra of *ca.* 100 nm occurs for all three morphologies, with the calculated spectra being blue-shifted with respect to the experimental ones, namely, 943 nm vs 1074 nm for the spheres, 983 nm vs 1069 nm for the rods, and 1007 nm vs 1103 nm for the tetrapods. This mismatch may be due to several factors related to the empirical dielectric function used as input data in the calculations in Figure 3 (I). Farag *et al.* determined the Cu_{2-x}Te dielectric function by averaging over multiple film thicknesses,⁴¹ and their R and T measurements clearly indicate a film thickness-dependent behavior. Thus, the use of a thickness-averaged dielectric function in our calculations might lead to the observed mismatch. Another factor relates to the thin-film XRD data from Farag *et al.*,⁴¹ which do not allow for an exact structural assignment. Hence, it is likely that the crystal structure of those thin films deviates from the weissite structure of our NCs. This would give rise to a deviation in the Cu deficiency, and thus to a dielectric mismatch that can originate a significant LSPR discrepancy between the experimental and calculated extinction spectra.

In the following we focus on the analysis of the calculated extinction spectra for the Cu_{2-x}Te nanorods. The inset in Figure 3b(I) schematically illustrates the excitation of the longitudinal (L-band hereafter, dashed arrow) and transverse (T-band hereafter, solid arrow) plasmon bands. The calculated L- (thin dashed line) and T-bands (thin solid line) are shown in Figure 3b(I). The T-band resembles the one for spherical particles, peaking at \sim 933 nm and approaching

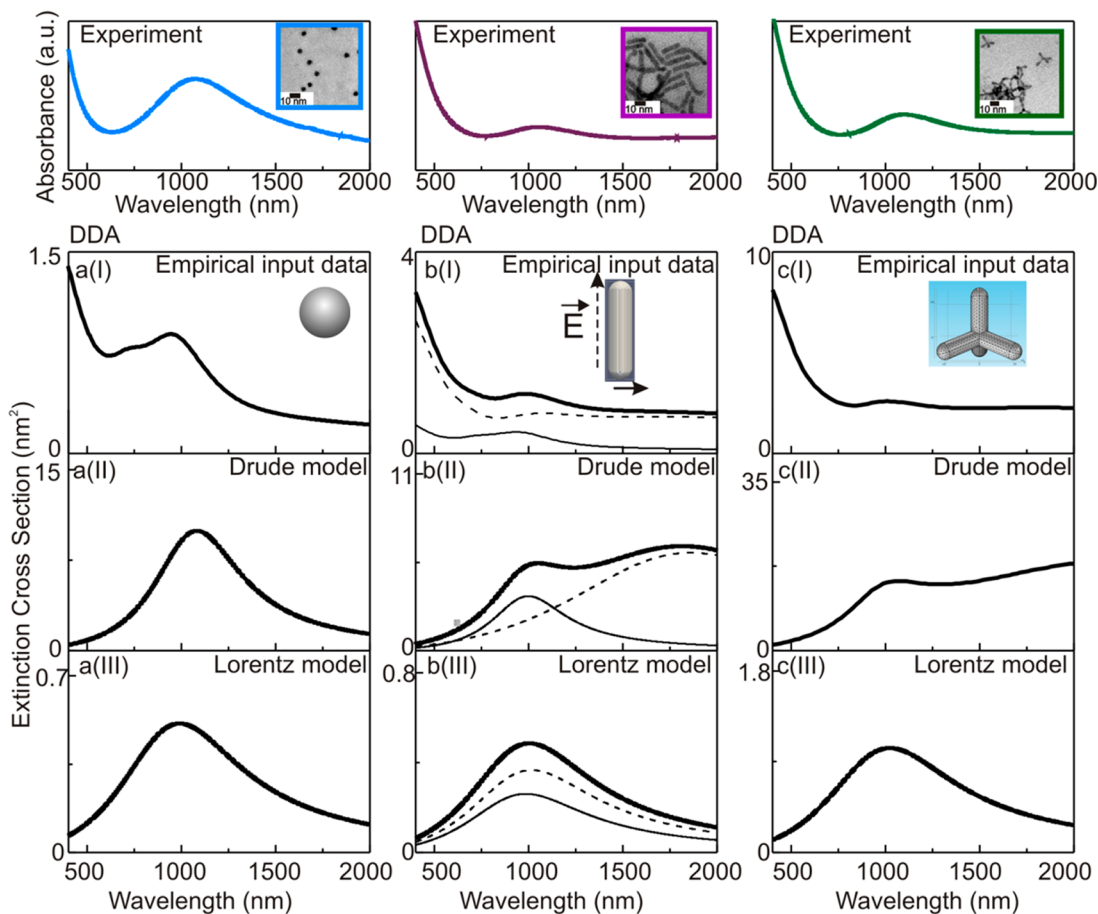


Figure 3. Top panel: experimental extinction spectra, given as a reference, of Cu_{2-x}Te spheres (blue curve, $\lambda_{\text{max}} = 1074 \text{ nm}$), nanorods (purple curve, $\lambda_{\text{max}} = 1069 \text{ nm}$), and tetrapods (green curve, $\lambda_{\text{max}} = 1103 \text{ nm}$). (I), (II), and (III) are the calculated (DDA) extinction spectra for a Cu_{2-x}Te (a) sphere ($d = 9 \text{ nm}$), (b) nanorod ($\text{length} \times \text{width}, L \times W = 21 \times 5 \text{ nm}$), and (c) tetrapod ($L \times W = 12 \times 5 \text{ nm}$). The spectra shown in (I) were calculated using an empirical dielectric function for Cu_{2-x}Te (ref 41) and have the following plasmon band maxima: a(I) sphere ($\lambda_{\text{max}} = 943 \text{ nm}$), b(I) nanorod ($\lambda_{\text{max}} = 983 \text{ nm}$) and c(I) tetrapod ($\lambda_{\text{max}} = 1007 \text{ nm}$). The spectra shown in (II) were calculated using the Drude model and the plasmon band maxima for the three shapes are a(II) sphere ($\lambda_{\text{max}} = 1090 \text{ nm}$), b(II) nanorod ($\lambda_{\text{max}} = 1050$ and 1284 nm) and c(II) tetrapod ($\lambda_{\text{max}} = 1068 \text{ nm}$). The spectra in (III) were calculated using the Lorentz model and have the following plasmon band maxima: a(III) sphere ($\lambda_{\text{max}} = 990 \text{ nm}$), b(III) nanorod ($\lambda_{\text{max}} = 1003 \text{ nm}$) and c(III) tetrapod ($\lambda_{\text{max}} = 1022 \text{ nm}$). In b(I), b(II), and b(III) the black thin solid curves represent the T-bands; the dashed thin curves represent the L-bands; and the black thick solid curves represent the averaged extinction spectra of the nanorods. All experimental spectra were measured in tetrachlorethylene as solvent, and thus, a dielectric constant of 1.505 was used for the surrounding medium in the simulations.

zero toward the red end of the spectrum. The L-band peaks at $\sim 1074 \text{ nm}$ and has an extended extinction in the NIR. Both bands are very close in energy despite the high aspect ratio (4.1) of the Cu_{2-x}Te nanorod (this differs with respect to a metallic nanorod of identical dimensions; see calculated extinction spectrum in Figure S10b, Supporting Information). Thus in the calculated averaged spectrum (thick solid curve, Figure 3b(I)) they result in a single plasmon band. Therefore, the intense plasmon band in the experimental spectra of the Cu_{2-x}Te nanorods (Figure 3-top panel, purple curve) is due to a contribution of the longitudinal and transverse plasmon resonances, while the broad extinction above *ca.* 1300 nm is primarily related to the L-band. Additional simulations (Figure S11 in the Supporting Information) demonstrate that by increasing the aspect ratio of a Cu_{2-x}Te nanorod while keeping its width (5 nm) and tip radius (2 nm) constant the T-band position

remains constant, while the L-band red shifts linearly and the broad NIR extinction becomes more and more dominant. These latter results indicate that plasmon damping gains in importance the lower the aspect ratio gets, *i.e.*, the more the nanorods approach the spherical case (see discussion below).

The results shown so far indicate only a weak shape dependence on the extinction spectra of the Cu_{2-x}Te NCs, while in strongly plasmonic nanoparticles, such as gold, the effect of NC shape can be more dramatic (see Figure S10a–c). This is due to strong electric fields that are very sensitive to the shape of the nanoparticle and boundary conditions. To further understand this finding and gain insights on the nature of the NIR optical resonances in our Cu_{2-x}Te nanocrystals, we simulated the extinction spectra for all three NC shapes using the model phenomenological dielectric functions given by eqs 1 (Drude model) and 2 (Lorentz model; see Experimental

Section). First, we will focus on the Drude dielectric function (eq 1) as input data (Figure 3 (II)). Physically, the Drude model assumes the presence of mobile carriers (holes) in Cu_{2-x}Te NCs. We determined this dielectric function by fitting the Mie resonance to the experimental extinction spectrum of our 9 nm diameter sphere. The best fit yielded the following fitting parameters: $\gamma = 0.6 \text{ eV}$, $\varepsilon_{\text{Cu}_{2-x}\text{Te},\infty} = 8.4$, and $\omega_p = 4.1 \text{ eV}$, where γ is the damping constant, $\varepsilon_{\text{Cu}_{2-x}\text{Te},\infty}$ is the high-energy dielectric constant of Cu_{2-x}Te , and ω_p its bulk plasma frequency (see Figure S12, solid curves, Supporting Information) and is represented in Figure 3a(II). The plasmon band shows a similar asymmetry to that of the experimental spectrum (Figure 3-top panel, blue curve) and peaks at 1090 nm (vs 1074 nm for the experiment). While the plasmon resonance is nicely reproduced for the spherical case, the interband transitions are clearly neglected in Drude's model. We used the same Drude dielectric function to simulate the extinction spectrum of a single $5 \times 21 \text{ nm}$ Cu_{2-x}Te nanorod. The average extinction spectrum is shown as a thick black curve in Figure 3b(II), while the contribution due to the transverse and longitudinal plasmon bands is given as thin solid and dashed curves, respectively. The averaged extinction spectrum shows two broad but distinct bands, the low-energy band being slightly more intense. Again, the band at *ca.* 1050 nm results from a contribution of the transverse (predominant in this case) and the longitudinal plasmon modes, while the band at *ca.* 1284 nm is mainly due to the longitudinal plasmon mode. However, while the high-energy plasmon resonance (T-band) determined from the Drude model qualitatively agrees with the one obtained after using the empirical dielectric function (Figure 3b(I)), the L-band is clearly overstated. Similar results are also found for the Cu_{2-x}Te tetrapod, where the Drude model overestimates the NIR region above *ca.* 1300 nm (Figure 3c(II)). We found a better agreement with the experimental spectra, when modifying the Drude model artificially by adding an additional damping term to our Drude dielectric function. This damping term acts only in the long-wavelength region (above 1000 nm; see Figures S12 and S13 in the Supporting Information for details) and thus forces the L-band to decrease in intensity. Furthermore, the L-band broadens, resulting in a pronounced residual extinction in the NIR, similar to the experimental spectra. This better agreement with the "damped" Drude model suggests that our NRs may have a significant damping contribution for oscillations above 1000 nm. On the other hand, the Lorentz dielectric function given by eq 2 corresponds to a regime opposite to the Drude picture since it treats particles (holes) as localized oscillators with a frequency Ω_L . Figure 3 (panel III) shows the extinction spectra obtained with a

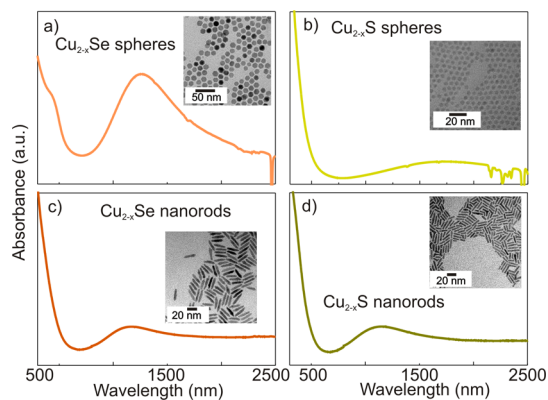


Figure 4. Experimental extinction spectra of Cu_{2-x}Se (a) spheres and (c) nanorods; and of Cu_{2-x}S (b) spheres and (d) nanorods. In both cases the spectra of the Cu_{2-x}Se and Cu_{2-x}S nanorods show a similar behavior to the spectrum of the Cu_{2-x}Te nanorods: a plasmon resonance at 1182 nm (Cu_{2-x}Se nanorods) and 1128 nm (Cu_{2-x}S nanorods) and broad extinction to the NIR resulting from a significant damping of the L-band. Note that the spherical Cu_{2-x}Se and Cu_{2-x}S NCs were prepared *via* one-pot synthesis, while Cu_{2-x}Se and Cu_{2-x}S nanorods were obtained by $\text{Cd}^{2+}/\text{Cu}^+$ from preformed CdSe/S nanorods, in analogy with the Cu_{2-x}Te presented throughout the article.

Lorentz dielectric function and the following fitting parameters: $\varepsilon_{\text{Cu}_{2-x}\text{Te},\infty} = 8.4$, $\Delta\varepsilon = 1$, $\Gamma_L = 1 \text{ eV}$, $\Omega_L = 1.2 \text{ eV}$ (see Figure S14 in the Supporting Information). Since the Lorentz model assumes localized carriers, the electric fields induced by such carriers are not strong, and, therefore, the extinction depends weakly on NC shape. The extinction cross section in this case depends mostly on the volume of the NCs and on $\text{Im}[\varepsilon_{\text{Cu}_{2-x}\text{Te},\text{Lorentz}}]$.

Physically, the results obtained by fitting with the model dielectric functions can be interpreted in the following way: the standard Drude model is not able to describe the set of data for all three NC shapes properly. The main difference between experiment and model is that the experiment does not show a significant L-band in the spectra of nanorods and tetrapods. However, a strong L-band is a very characteristic feature of Drude-like free carriers (holes in this case) in elongated nanoparticles (see Figure S10b in the Supporting Information for gold nanorods). This is a very important observation. Further, when we use the Lorentz model of localized quantum particles, we obtain an overall reasonable description of the experiment. Nevertheless, also with this model the increased extinction background in the interval of $\sim 1300\text{--}3000 \text{ nm}$ (see experimental results in Figure 3-top panel, purple and green curves, respectively) is not fully represented. However, with the introduction of an artificial increased damping at longer wavelengths into the Drude model, we can suppress the L-band in the calculated extinction spectra and the modeled spectra become closer to the experimental data. These observations suggest that the holes in the valence band of

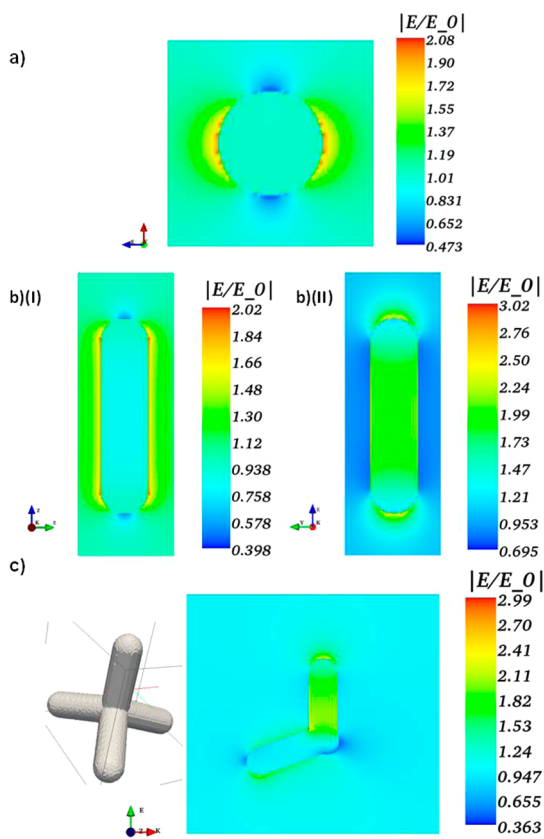


Figure 5. Near-field enhancement maps for a Cu_{2-x}Te sphere, nanorod, and tetrapod upon excitation at their respective resonance frequencies (determined from Figure 3(I)): (a) sphere, excited at 943 nm, (b) rod (I) T-band and (II) L-band excited at 933 and 1074 nm, respectively, and (c) tetrapod excited at 1007 nm.

Cu_{2-x}Te NCs have an essential degree of localization. Similar observations for other copper chalcogenides (Cu_{2-x}S and Cu_{2-x}Se nanospheres and nanorods; see extinction spectra in Figure 4) suggest an essential degree of localization of holes in those NCs as well and, thus, that the Lorentz-type behavior of holes is a general property of copper chalcogenide NCs. We should note that the effect of localization of carriers in bulk semiconductors with disorder has been intensively studied in the past.⁴³ A disordered bulk semiconductor can exhibit a so-called mobility edge.⁴³ All electron states below the mobility-edge energy in the conduction band of an n-type semiconductor are localized. Similarly, all hole states above the mobility edge in the valence band of a p-type semiconductor become localized. In a bulk semiconductor, if the Fermi energy is close to the mobility edge, an essential part of the carriers in a semiconductor is localized. In our case, we deal with holes that have an essential degree of localization according to the measured plasmonic responses. We also note that the concepts of bulk disordered semiconductors are applicable to nanostructures if a localization length of a carrier is shorter than the size of a nanostructure. In this case, a carrier

cannot move freely inside a nanostructure. The results presented here suggest that the simple plasmonic Drude-like picture may not be sufficient to understand Cu_{2-x}Te and similar NCs, and further investigations are needed. The behavior of a NC (Drude-like vs Lorentz-like) may depend on the synthesis method and NC dimensions. Nevertheless, in our case a comparison of the extinction spectra of Cu_{2-x}S nanorods obtained via one-pot synthesis vs Cu_{2-x}S nanorods obtained via cation exchange (results not shown) shows that the degree of plasmon damping in the high-wavelength interval is very similar in both cases. This suggests that the effect of material quality (crystallinity, etc.) is not very critical in our experiments (at least for the Cu_{2-x}S nanorods examined herein). However, effects such as plasmon damping and hole localization can potentially depend on the crystallinity, synthesis strategy, and disorder.

We now return to the empirical dielectric function taken from ref 41 and evaluate the computed electric near-fields of optically driven Cu_{2-x}Te NCs. In Figure 5 the near-field enhancement (NFE) maps for all three shapes investigated herein are given. Excitation of the Cu_{2-x}Te sphere (Figure 5a) at its resonance wavelength (943 nm, as determined from Figure 3a(I)) shows a clear dipolar-like character, confirming that the fit to the spherical extinction spectrum of the spheres using the Mie formula in the dipolar approximation is valid for a 9 nm Cu_{2-x}Te sphere. For our 21×5 nm Cu_{2-x}Te nanorod the NFE maps shown in Figure 5 indicate that upon excitation at 933 nm (T-band in Figure 3b(I)) a dipolar-like NFE pattern is induced along the nanorod short axis (Figure 5b(I)), while excitation at 1074 nm (L-band in Figure 3b(II)) induces a dipolar-like electric field enhancement along the major axis of the nanorod (Figure 5b(II)). On the other hand, the NFE map of our 12×5 nm tetrapod upon excitation at 1007 nm, given in Figure 5c, shows that the dipole in the plane of excitation is mainly located at the tip of the excited arm. However, part of it is scattered into another arm. In all three cases the NFE factors for Cu_{2-x}Te NCs are very low, especially when compared to plasmonic nanoparticles of noble metals. The NFE of the Cu_{2-x}Te sphere and of the nanorod after excitation of the T-band stay at the lower end (with a NFE of *ca.* 2), while the tetrapod and the nanorod (L-band excitation) give the highest NFE (*ca.* 3). In any case, the NFE for the L-band of the Cu_{2-x}Te nanorod is about 30 times lower than that of a gold nanorod of the same dimensions (see Figure S10d). This might be explained by a *ca.* $100 \times$ lower carrier density for Cu_{2-x}Te .² However, an influence from carrier localization cannot be excluded here.

CONCLUSIONS

In this work we presented a straightforward strategy to prepare Cu_{2-x}Te NCs of well-defined shapes

(spheres, rods, and tetrapods) *via* Cd²⁺/Cu⁺ exchange from preformed CdTe NCs. The process occurs along with morphology preservation, and thus we envisage any other shape as conceivable. All synthesized Cu_{2-x}Te NCs show pronounced plasmon bands in the NIR. Modeling the optical response of those NCs with the DDA and using an empirical dielectric function as input data delivered a qualitatively good agreement with the experimental results. Our modeling by the phenomenological dielectric functions (standard Drude, modified Drude, and Lorentz models) suggests

that the standard Drude model does not work well for Cu_{2-x}Te NCs of various shapes; that damping above *ca.* 1000 nm is non-negligible for nanorods and tetrapods; and that some localization of carriers occurs in the valence band of Cu_{2-x}Te, which may be a common property for the whole copper chalcogenide family. In summary, our results represent a simple route toward copper telluride NCs with well-defined morphologies and NIR plasmonic resonances and provide a clearer understanding of the NIR optical resonances of vacancy-doped copper chalcogenide NCs.

EXPERIMENTAL SECTION

Synthesis of Cd-Based NCs. For the synthesis of CdTe NCs of various shapes (spheres, rods, and tetrapods) and CdS and CdSe nanorods, selenium powder (Se), tellurium (Te), cadmium oxide (CdO), trioctylphosphine (TOP), tributylphosphine (TBP), *n*-tetradecylphosphonic acid (TDPA), octadecene (ODE), octadecylphosphonic acid (ODPA), trioctylphosphine oxide (TOPO), and oleic acid (OA) were purchased from Sigma-Aldrich and used as received. All solvents used were anhydrous solvents of high purity purchased from Sigma-Aldrich. Syntheses were performed using standard air-free Schlenk line techniques.

a. Synthesis of CdTe Spheres. A modified synthesis for CdTe NCs was used.⁴⁴ The Te precursor solution was prepared by dissolving 0.501 g of Te in 10.8 mL of TOP. The mixture was stirred for 30 min at 275 °C on a hot plate until the solution turned yellow. Remaining solid parts were removed *via* centrifugation for synthesis. The Cd precursor was prepared by mixing 102 mg of CdO, 3.204 g of TOPO, and 0.796 g of ODPA in a 50 mL three-neck flask. The mixture was degassed at 120 °C for 30 min and heated to 300 °C under nitrogen flow until the solution turned clear, indicating that the Cd precursor was formed. At 300 °C 1.8 mL of TOP was injected, and the temperature was further increased to 320 °C for the injection of 0.54 mL of the Te-TOP precursor. The temperature dropped to 315 °C after injection and was maintained for a further 7 min at 315 °C. Subsequently, the heating mantle was removed. After cooling to 70 °C, 10 mL of anhydrous toluene was added to the flask, and the dispersion was transferred to a nitrogen-filled glovebox. The nanocrystals were precipitated twice by the addition of anhydrous methanol and redispersed in anhydrous toluene. Thereafter the particles were stored in a N₂-filled glovebox.

b. Synthesis of CdTe Nanorods. For the preparation of CdTe nanorods, we pursued two different synthetic approaches:

A Te injection solution containing 0.120 g of Te was prepared in a glovebox by dissolving Te powder in 1320 μL of TBP and then diluted with 9 mL of ODE. A mixture of CdO (0.08 g), OA (820 μL), and ODE (5 mL) was heated in a three-neck flask to 120 °C and kept at this temperature for 1 h under vacuum. The Cd precursor solution was then heated to 300 °C to obtain a clear solution. At this temperature, the Te injection solution was quickly injected into the hot solution. The reaction mixture was allowed to cool to 260 °C for the growth of the CdTe nanocrystals for 7 min. Thereafter the solution was allowed to cool naturally. For sample washing, the colloidal solution was first diluted with 7 mL of hexane. Thereafter the NCs were precipitated with 14 mL of methanol and centrifuged at 4000 rpm for 5 min. A second washing cycle was performed by addition of 20 mL of acetone to 15 mL of the NCs in toluene. The supernatant was discarded, and the NCs were redispersed in 15 mL of toluene. The NC solution was dried under vacuum and transferred to a N₂-filled glovebox. The NCs were finally redispersed in anhydrous toluene and kept under N₂ for further experiments.⁴⁵

Alternatively, CdTe nanorods were synthesized following a literature procedure described elsewhere in detail.⁴⁶ The Cd precursor was prepared by degassing a mixture of 0.114 g of

CdO, 0.43 g of TDPA, and 7 g of TOPO at 120 °C for 1 h. The mixture was heated to 350 °C under nitrogen until the solution turned clear. The Te precursor solution was prepared by dissolving 0.255 g of Te in 10 mL of TOP (*c* = 0.2 M) under rigorous stirring at 150 °C for about 1 h in a N₂-filled glovebox. The temperature of the Cd precursor solution was lowered to 290 °C for injection of 0.5 mL of the Te-TOP precursor. The temperature dropped to 280 °C after injection. Thereafter the temperature was increased to 300 °C, followed by the subsequent injection of 0.5 mL of Te-TOP solutions every 2 min until a total of 4 mL was injected. After reaction the solution was allowed to cool to 70 °C, when 15 mL of anhydrous toluene was added to the reaction mixture by syringe. The resulting solution was transferred to a glovebox. The NCs were precipitated twice with 30 mL of anhydrous ethanol and centrifugation (6000 rpm, 5 min). Finally the NCs were redispersed in 10 mL of anhydrous toluene.

c. Synthesis of CdTe Tetrapods. A typical synthesis of CdTe tetrapods was undertaken following a modified procedure of Yu *et al.*⁴⁵ In detail, in a three-necked 25 mL flask a mixture of 0.6 mmol of CdO and 2.4 mmol of OA in 8 mL of ODE was heated to 100 °C under vacuum for 30 min to remove any residual oxygen and moisture. Under inert (Ar) atmosphere, this mixture was further heated to 300 °C until a clear, colorless solution was obtained. After cooling this solution to 280 °C a freshly prepared mixture of 0.6 mmol of Te in 0.6 mL of TOP and 1.4 mL of ODE was quickly injected. The solution was kept at 250 °C for 5 min before it was cooled to room temperature by direct placement into a room-temperature water bath underneath and injection of 6 mL of toluene. The tetrapods were then purified by precipitation with a 2-propanol/methanol mixture and redispersed in toluene. For further use the NCs were dried into a powder and transferred into a glovebox. The NCs were redispersed in anhydrous toluene and stored under N₂ for later use.

d. Synthesis of CdSe Nanorods. CdSe nanorods were synthesized following ref 47. The cadmium precursor solution was prepared by mixing 1.6 mmol of CdO (0.205 g), 3.2 mmol of TDPA (0.89 g), and 3.11 g of TOPO in a three-neck flask and heating to 120 °C for about 10 min under vacuum. Thereafter the temperature was increased to 310 °C under N₂ flow until the solution turned clear. The mixture was kept at this temperature for 10 min before the flask was cooled to room temperature and aged for about 24 h in a N₂ atmosphere. The selenium injection solution as prepared by mixing 0.8 mmol of Se powder (63 mg) with 190 mg of TBP (0.463 mL), 1.447 g of TOP (0.483 mL), and 0.3 g of toluene (0.347 mL) in a N₂-filled glovebox. The Cd-precursor solution was heated to 320 °C under nitrogen, when the Se-TBP-TOP solution was injected into the reaction flask, followed by a temperature drop to 300 °C, where the reaction mixture was kept for 8 min. During reaction a gradual color change from light orange to dark red and black was observed. The heating mantle was removed, and the flask was allowed to cool to 70 °C, when 5 mL of anhydrous toluene was injected into the flask. The reaction solution was transferred into the N₂-filled glovebox for further purification. A 15 mL amount of anhydrous toluene and methanol was added to flocculate the nanocrystals

followed by centrifugation (6000 rpm, 5 min) and decantation. The supernatant was discarded and the precipitate redissolved. The washing process was repeated five times to remove all reaction chemicals from the solution. Finally, the precipitate containing the CdSe nanorods was dispersed in 2 mL of toluene and stored in the N₂-filled glovebox for further use.

CdS Nanorods. CdS nanorods were prepared following ref 48. The cadmium precursor solution was prepared by mixing 0.23 g of CdO (1.8 mmol), 0.83 g of TDPA (3.0 mmol), and 7 g of trioctylphosphine oxide (99%) followed by degassing for 1 h at 80 °C. Thereafter the flask was heated to 340 °C under N₂ flow, when color changed from dark red to clear, indicating the formation of the Cd–TDPA complex. After cooling to 300 °C, the sulfur precursor solution, prepared by dissolving 0.18 g of sulfur powder in 20 mL of TOP, was injected into the reaction solution in steps of 0.4 mL each, every 2 min. Washing was performed by adding a nonsolvent such as ethanol followed by precipitation and decantation. The NCs were redispersed in toluene and kept for further use.

Ion Exchange. For ion exchange tetrakis(acetonitrile)copper(I) hexafluorophosphate ($[(CH_3CN)_4Cu]PF_6$) was purchased from Sigma Aldrich. All steps were performed in a N₂-filled glovebox with anhydrous solvents. Oleylamine was acquired from Sigma Aldrich and degassed for 24 h before use.

For the ion exchange reaction the Cd concentration of the corresponding CdTe NC stock solution was estimated from the absorbance of the first excitonic peak as described in ref 38. An exact amount of NC stock solution was diluted for extinction measurements. The concentration of the diluted solution was determined using the formulas following ref 38. Reference 38 is strictly valid only for spherical particles. Nevertheless, it gave an upper limit to determine the amount of Cu⁺ that has to be added to the solution. This was chosen to be an approximate 10× stoichiometric excess. The Cu⁺ stock solution was prepared in the glovebox by dissolving tetrakis(acetonitrile)copper(I) hexafluorophosphate ($[(Cu(CH_3CN)_4]PF_6$) in anhydrous methanol to a concentration of 4 mg/mL. For ion exchange typically a mixture of 0.75 mL of Cu⁺ stock solution, 0.75 mL of methanol, and 1.5 mL of toluene was rapidly stirred. Then 60 μ L of the Cu⁺ stock solution ($\sim 6 \times 10^{-5}$ mol/L) was added. An immediate color change from dark brown to golden indicated that the ion exchange occurred immediately. The solution was kept stirring for another 2 min before centrifugation at 4000 rpm for 5 min. The supernatant containing the exchanged Cd²⁺ ions and remaining Cu⁺ ions was discarded. The dark brown precipitate containing the ion-exchanged NCs was redispersed in 1 mL of anhydrous toluene or TCE for further experiments. Without further treatment the NCs tend to aggregate after ion exchange. For optical analysis colloidal stability of the NCs is essential. Therefore, clustering of Cu_{2-x}Te NCs was prevented by the addition of ligands in excess during the exchange process. For this 200 μ L of oleylamine was added to the mixture before the addition of the corresponding NC stock solution. After precipitation the excess ligands remain in the supernatant and are subsequently discarded. No differences in the optical spectra were observed when excess ligands were added to the dispersion after synthesis. Note that the addition of dodecanthiol (DDT) as ligand prevented the ion exchange, probably because DDT strongly binds to the Cu⁺ ions in solution, preventing the ion exchange reaction.

Optical Characterization. UV–vis–NIR extinction spectra of all NCs were measured in 1 cm path length NIR quartz cuvettes using a Cary 5000 UV–vis–NIR spectrophotometer. For these experiments a dilute dispersion of NCs was prepared inside a N₂-filled glovebox using anhydrous solvents. For measurements in the NIR TCE was used as a solvent to allow for NIR extinction measurements without interference from the solvent. To avoid any solvent peaks in the spectrum the NC solution in TCE was kept on a hot plate at around 70 °C in the N₂-filled glovebox to ensure that any remaining solvent from synthesis is evaporated. For optical measurement 300 μ L of the ion-exchanged NC sample was diluted with 2 mL of solvent. To reach the maximum copper vacancy density (given by the maximum plasmon resonance) for all NCs, the NC dispersions were kept at ambient conditions until no spectral changes were observed.⁸ In a typical

PL steady-state experiment, the NCs were excited at 400 nm by a monochromated Xe lamp, and a long-pass glass filter (Schott OG590) was used to cut the excitation wavelength. PL spectra were obtained with a double monochromator fluorometer (Jobin-Yvon) equipped with a water-cooled detector sensitive in the NIR spectral range down to 1000 nm.

Structural Characterization. Wide-angle powder X-ray diffraction patterns were collected using a Bruker D8 diffractometer with a Cu K α X-ray source operating at 40 kV and 40 mA and a Vantec 2000 area detector. The assignment of crystalline phases was based on the reference files in the Powder Diffraction File (PDF-2) database from International Center for Diffraction Data. For XRD the precipitated NCs were redispersed in a very low amount of solvent and dropped onto a cover slit in 5 μ L drops until the layer was thick enough to give a reasonable XRD signal. The cover slit was placed on a hot plate at \sim 100 °C to allow the solvent to evaporate faster.

TEM. For TEM, typically 5 μ L of the corresponding NC solution was drop-casted on a carbon-coated Cu TEM grid. For EDX measurements, Au grids were used. Remaining solvent was removed with a filter paper. A FEI Titan 80-300 equipped with a Gatan Tridiem and EDAX ultrathin window Si (Li) EDX detector was used at 300 kV.

Optical Modeling. To compute the optical spectra of the Cu_{2-x}Te NCs, we employed both experimental and model dielectric functions. The experimental dielectric function of Cu_{2-x}Te was taken from ref 41. The model dielectric functions used were of two types:

$$\varepsilon_{\text{Drude, Cu}_{2-x}\text{Te}} = \varepsilon_{\text{Cu}_{2-x}\text{Te}, \infty} - \frac{\omega_p^2}{\omega(\omega + \gamma_D)} \quad (1)$$

and

$$\varepsilon_{\text{Lorentz, Cu}_{2-x}\text{Te}} = \varepsilon_{\text{Cu}_{2-x}\text{Te}, \infty} - \frac{\Delta\epsilon\Omega_L^2}{(\omega^2 - \Omega_L^2) + i\omega\Gamma_L} \quad (2)$$

where ω_p is the plasmon frequency in the Drude model and Ω_L is the discrete transition frequency in the Lorentz model,⁴⁹ and the other parameters, γ_D and Γ_L , describe the broadening of plasmon resonances and the oscillator strength of the transition ($\Delta\epsilon$), respectively. These two models correspond to two different physical situations. The Drude model describes a system of free carriers in a crystal, whereas the Lorentz model is valid for localized carriers or for interband transitions. In our case, we will try the above equations (eqs 1 and 2) as phenomenological models to describe NIR optical excitations of holes in the valence band of Cu_{2-x}Te.

The computational results given below are based on a numerical solution of Maxwell's equations incorporating local dielectric functions of Cu_{2-x}Te and a solvent medium. As a numerical method, we employed the discrete dipole approximation^{50–52} and the software from refs 53 and 54. The DDA code was taken from the open source at ref 53.

Conflict of Interest: The authors declare no competing financial interest.

Supporting Information Available: Size distribution of Cu_{2-x}Te spheres, rods, and tetrapods (Figures S1–S3); photoluminescence spectra of CdTe and Cu_{2-x}Te nanorods (Figure S4); XRD patterns of Cu_{2-x}Te spheres, rods, and tetrapods (Figure S5); vis–NIR extinction and FTIR spectra of Cu_{2-x}Te nanorods (21 \times 5 nm) (Figure S6); extinction spectra of Cu_{2-x}Te nanorods of 5.5 \times 48 nm (width \times length, AR = 9.6) (Figure S7); 2D sketch of the Cu_{2-x}Te geometry used as input data in the simulations (Figure S8); empirical dielectric function of Cu_{2-x}Te from Farag *et al.*⁴¹ (Figure S9); calculated (DDA) extinction spectra of a 9 nm diameter Au sphere and of a 5 \times 21 nm Au nanorod (including electric field enhancement map) (Figure S10); effect of increasing the length of a Cu_{2-x}Te nanorod on its calculated (DDA) extinction spectrum (Figure S11); Drude and Drude-damped dielectric functions (Figure S12); calculated (DDA) extinction spectrum of a 5 \times 21 Cu_{2-x}Te nanorod using an artificially damped Drude-like dielectric function (Figure S13); Lorentz dielectric function (Figure S14). This material is available free of charge via the Internet at <http://pubs.acs.org>.

Acknowledgment. J.F., J.R.F., and I.K. acknowledge the Bavarian Ministry of Science, Research and Arts for financial support through the project Solar Technologies Go Hybrid (SoTech). The Nanosystems Initiative Munich (NIM) of the DFG is kindly acknowledged. J.R.F. acknowledges funding from the European Commission through the FP7-NMP programme (project UNION, grant agreement no. 310250). H.Z. and A.O.G. were supported by the U.S. Army Research Office under contract/grant number W911NF-12-1-0407 and by Volkswagen Foundation (Germany). Use of the Center for Nanoscale Materials by A.O.G and H.Z was supported by the U. S. Department of Energy, Office of Science, Office of Basic Energy Sciences, under Contract No. DE-AC02-06CH11357. The electron microscopy studies and structural characterization were performed at the Department of Chemistry and CeNS, Ludwig-Maximilians-Universität München. The assistance of Prof. Christina Scheu on the structural characterization of the material is greatly acknowledged. We are grateful to Maximilian Berr and Joanna Kolny-Olesiak for providing some test samples. Graphical support from Christoph Hohmann (NIM) is greatly appreciated.

REFERENCES AND NOTES

- Li, S.; Wang, H.; Xu, W.; Si, H.; Tao, X.; Lou, S.; Du, Z.; Li, L. S. Synthesis and Assembly of Monodisperse Spherical Cu₂S Nanocrystals. *J. Colloid Interface Sci.* **2009**, *330*, 483–487.
- Luther, J. M.; Jain, P. K.; Ewers, T.; Alivisatos, A. P. Localized Surface Plasmon Resonances Arising from Free Carriers in Doped Quantum Dots. *Nat. Mater.* **2011**, *10*, 361–366.
- Kruszynska, M.; Borchert, H.; Bachmatiuk, A.; Rümmeli, M. H.; Büchner, B.; Parisi, J.; Kolny-Olesiak, J. Size and Shape Control of Colloidal Copper(I) Sulfide Nanorods. *ACS Nano* **2012**, *6*, 5889–5896.
- Dorfs, D.; Härtling, T.; Miszta, K.; Bigall, N. C.; Kim, M. R.; Genovese, A.; Falqui, A.; Povia, M.; Manna, L. Reversible Tunability of the Near-Infrared Valence Band Plasmon Resonance in Cu_{2-x}Se Nanocrystals. *J. Am. Chem. Soc.* **2011**, *133*, 11175–11180.
- Hsu, S.-W.; On, K.; Tao, A. R. Localized Surface Plasmon Resonances of Anisotropic Semiconductor Nanocrystals. *J. Am. Chem. Soc.* **2011**, *133*, 19072–19075.
- Hsu, S.-W.; Bryks, W.; Tao, A. R. Effects of Carrier Density and Shape on the Localized Surface Plasmon Resonances of Cu_{2-x}S Nanodisks. *Chem. Mater.* **2012**, *24*, 3765–3771.
- Kriegel, I.; Rodríguez-Fernández, J.; Como, E. D.; Lutich, A. A.; Szeifert, J. M.; Feldmann, J. Tuning the Light Absorption of Cu_{1.9}S Nanocrystals in Supercrystal Structures. *Chem. Mater.* **2011**, *23*, 1830–1834.
- Kriegel, I.; Jiang, C.; Rodríguez-Fernández, J.; Schaller, R. D.; Talapin, D. V.; da Como, E.; Feldmann, J. Tuning the Excitonic and Plasmonic Properties of Copper Chalcogenide Nanocrystals. *J. Am. Chem. Soc.* **2012**, *134*, 1583–1590.
- Scotognella, F.; Della Valle, G.; Srimath Kandada, A. R.; Dorfs, D.; Zavelani-Rossi, M.; Conforti, M.; Miszta, K.; Comin, A.; Korobchevskaya, K.; Lanzani, G.; et al. Plasmon Dynamics in Colloidal Cu_{2-x}Se Nanocrystals. *Nano Lett.* **2011**, *11*, 4711–4717.
- Zhao, Y.; Burda, C. Development of Plasmonic Semiconductor Nanomaterials with Copper Chalcogenides for a Future with Sustainable Energy Materials. *Energy Environ. Sci.* **2012**, *5*, 5564–5576.
- Routzahn, A. L.; White, S. L.; Fong, L.-K.; Jain, P. K. Plasmonics with Doped Quantum Dots. *Isr. J. Chem.* **2012**, *52*, 983–991.
- Scotognella, F.; Valle, G. D.; Kandada, A. R. S.; Zavelani-Rossi, M.; Longhi, S.; Lanzani, G.; Tassone, F. Plasmonics in Heavily-Doped Semiconductor Nanocrystals. *Eur. Phys. J. B* **2013**, *86*, 154.
- Zhao, Y.; Pan, H.; Lou, Y.; Qiu, X.; Zhu, J.; Burda, C. Plasmonic Cu_{2-x}S Nanocrystals: Optical and Structural Properties of Copper-Deficient Copper(I) Sulfides. *J. Am. Chem. Soc.* **2009**, *131*, 4253–4261.
- Li, W.; Shavel, A.; Guzman, R.; Rubio-Garcia, J.; Flox, C.; Fan, J.; Cadavid, D.; Ibanez, M.; Arbiol, J.; Morante, J. R.; et al. Morphology Evolution of Cu_{2-x}S Nanoparticles: From Spheres to Dodecahedrons. *Chem. Commun.* **2011**, *47*, 10332–10334.
- Wu, Y.; Wadia, C.; Ma, W.; Sadler, B.; Alivisatos, A. P. Synthesis and Photovoltaic Application of Copper(I) Sulfide Nanocrystals. *Nano Lett.* **2008**, *8*, 2551–2555.
- Zhuang, Z.; Peng, Q.; Zhang, B.; Li, Y. Controllable Synthesis of Cu₂S Nanocrystals and Their Assembly into a Superlattice. *J. Am. Chem. Soc.* **2008**, *130*, 10482–10483.
- Brelle, M. C.; Torres-Martinez, C. L.; McNulty, J. C.; Mehra, R. K.; Zhang, J. Z. Synthesis and Characterization of Cu_xS Nanoparticles. Nature of the Infrared Band and Charge-Carrier Dynamics. *Pure Appl. Chem.* **2000**, *72*, 101–117.
- Haram, S. K.; Mahadeshwar, A. R.; Dixit, S. G. Synthesis and Characterization of Copper Sulfide Nanoparticles in Triton-X 100 Water-in-Oil Microemulsions. *J. Phys. Chem.* **1996**, *100*, 5868–5873.
- Riha, S. C.; Johnson, D. C.; Prieto, A. L. Cu₂Se Nanoparticles with Tunable Electronic Properties Due to a Controlled Solid-State Phase Transition Driven by Copper Oxidation and Cationic Conduction. *J. Am. Chem. Soc.* **2011**, *133*, 1383–1390.
- Deka, S.; Genovese, A.; Zhang, Y.; Miszta, K.; Bertoni, G.; Krahne, R.; Giannini, C.; Manna, L. Phosphine-Free Synthesis of p-Type Copper(I) Selenide Nanocrystals in Hot Coordinating Solvents. *J. Am. Chem. Soc.* **2010**, *132*, 8912–8914.
- Larsen, T. H.; Sigman, M.; Ghezelbash, A.; Doty, R. C.; Korgel, B. A. Solventless Synthesis of Copper Sulfide Nanorods by Thermolysis of a Single Source Thiolate-Derived Precursor. *J. Am. Chem. Soc.* **2003**, *125*, 5638–5639.
- Sigman, M. B.; Ghezelbash, A.; Hanrath, T.; Saunders, A. E.; Lee, F.; Korgel, B. A. Solventless Synthesis of Monodisperse Cu₂S Nanorods, Nanodisks, and Nanoplatelets. *J. Am. Chem. Soc.* **2003**, *125*, 16050–16057.
- Saunders, A. E.; Ghezelbash, A.; Smilgies, D.-M.; Sigman, M. B.; Korgel, B. A. Columnar Self-Assembly of Colloidal Nanodisks. *Nano Lett.* **2006**, *6*, 2959–2963.
- Li, H.; Brescia, R.; Krahne, R.; Bertoni, G.; Alcocer, M. J. P.; D'Andrea, C.; Scotognella, F.; Tassone, F.; Zanella, M.; De Giorgi, M.; et al. Blue-UV-Emitting ZnSe(Dot)/ZnS(Rod) Core/Shell Nanocrystals Prepared from CdSe/CdS Nanocrystals by Sequential Cation Exchange. *ACS Nano* **2012**, *6*, 1637–1647.
- Zhang, Y.; Qiao, Z.-P.; Chen, X.-M. Microwave-Assisted Elemental Direct Reaction Route to Nanocrystalline Copper Chalcogenides CuSe and Cu₂Te. *J. Mater. Chem.* **2002**, *12*, 2747–2748.
- Jiang, L.; Zhu, Y.-J.; Cui, J.-B. Nanostructures of Metal Tellurides (PbTe, CdTe, CoTe₂, Bi₂Te₃, and Cu₇Te₄) with Various Morphologies: A General Solvothermal Synthesis and Optical Properties. *Eur. J. Inorg. Chem.* **2010**, *2010*, 3005–3011.
- Palchik, O.; Kerner, R.; Zhu, Z.; Gedanken, A. Preparation of Cu_{2-x}Te and HgTe by Using Microwave Heating. *J. Solid State Chem.* **2000**, *154*, 530–534.
- Li, B.; Xie, Y.; Huang, J.; Liu, Y.; Qian, Y. Sonochemical Synthesis of Nanocrystalline Copper Tellurides Cu₇Te₄ and Cu₄Te₃ at Room Temperature. *Chem. Mater.* **2000**, *12*, 2614–2616.
- Rivest, J. B.; Jain, P. K. Cation Exchange on the Nanoscale: an Emerging Technique for New Material Synthesis, Device Fabrication, and Chemical Sensing. *Chem. Soc. Rev.* **2013**, *42*, 89–96.
- Son, D. H.; Hughes, S. M.; Yin, Y.; Paul Alivisatos, A. Cation Exchange Reactions in Ionic Nanocrystals. *Science* **2004**, *306*, 1009–1012.
- Jain, P. K.; Amirav, L.; Aloni, S.; Alivisatos, A. P. Nanoheterostructure Cation Exchange: Anionic Framework Conservation. *J. Am. Chem. Soc.* **2010**, *132*, 9997–9999.
- Robinson, R. D.; Sadler, B.; Demchenko, D. O.; Erdonmez, C. K.; Wang, L.-W.; Alivisatos, A. P. Spontaneous Superlattice Formation in Nanorods through Partial Cation Exchange. *Science* **2007**, *317*, 355–358.
- Sadler, B.; Demchenko, D. O.; Zheng, H.; Hughes, S. M.; Merkle, M. G.; Dahmen, U.; Wang, L.-W.; Alivisatos, A. P.

Selective Facet Reactivity during Cation Exchange in Cadmium Sulfide Nanorods. *J. Am. Chem. Soc.* **2009**, *131*, 5285–5293.

34. Luther, J. M.; Zheng, H.; Sadler, B.; Alivisatos, A. P. Synthesis of PbS Nanorods and Other Ionic Nanocrystals of Complex Morphology by Sequential Cation Exchange Reactions. *J. Am. Chem. Soc.* **2009**, *131*, 16851–16857.

35. Deka, S.; Miszta, K.; Dorfs, D.; Genovese, A.; Bertoni, G.; Manna, L. Octapod-Shaped Colloidal Nanocrystals of Cadmium Chalcogenides via “One-Pot” Cation Exchange and Seeded Growth. *Nano Lett.* **2010**, *10*, 3770–3776.

36. Li, H.; Zanella, M.; Genovese, A.; Povia, M.; Falqui, A.; Giannini, C.; Manna, L. Sequential Cation Exchange in Nanocrystals: Preservation of Crystal Phase and Formation of Metastable Phases. *Nano Lett.* **2011**, *11*, 4964–4970.

37. Miszta, K.; Dorfs, D.; Genovese, A.; Kim, M. R.; Manna, L. Cation Exchange Reactions in Colloidal Branched Nanocrystals. *ACS Nano* **2011**, *5*, 7176–7183.

38. Yu, W. W.; Qu, L.; Guo, W.; Peng, X. Experimental Determination of the Extinction Coefficient of CdTe, CdSe, and CdS Nanocrystals. *Chem. Mater.* **2003**, *15*, 2854–2860.

39. Esch, V.; Fluegel, B.; Khitrova, G.; Gibbs, H. M.; Xu, J.; Kang, K.; Koch, S. W.; Liu, L. C.; Risbud, S. H.; Peyghambarian, N. State Filling, Coulomb, and Trapping Effects in the Optical Nonlinearity of CdTe Quantum Dots in Glass. *Phys. Rev. B* **1990**, *42*, 7450–7453.

40. Rowe, D. J.; Jeong, J. S.; Mkhoyan, K. A.; Kortshagen, U. R. Phosphorus-Doped Silicon Nanocrystals Exhibiting Mid-Infrared Localized Surface Plasmon Resonance. *Nano Lett.* **2013**, *13*, 1317–1322.

41. Farag, B. S.; Khodier, S. A. Direct and Indirect Transitions in Copper Telluride Thin Films. *Thin Solid Films* **1991**, *201*, 231–240.

42. Rajkanan, K. Determination of Stoichiometry of Thin Films of Cu₂– α S from their Optical Properties. *Mater. Res. Bull.* **1979**, *14*, 207–216.

43. Mott, N. The Mobility Edge since 1967. *J. Phys. C: Solid State Phys.* **1987**, *20*, 3075.

44. Manna, L.; Milliron, D. J.; Meisel, A.; Scher, E. C.; Alivisatos, A. P. Controlled Growth of Tetrapod-Branched Inorganic Nanocrystals. *Nat. Mater.* **2003**, *2*, 382–385.

45. Yu, W. W.; Wang, Y. A.; Peng, X. Formation and Stability of Size-, Shape-, and Structure-Controlled CdTe Nanocrystals: Ligand Effects on Monomers and Nanocrystals. *Chem. Mater.* **2003**, *15*, 4300–4308.

46. Shieh, F.; Saunders, A. E.; Korgel, B. A. General Shape Control of Colloidal CdS, CdSe, CdTe Quantum Rods and Quantum Rod Heterostructures. *J. Phys. Chem. B* **2005**, *109*, 8538–8542.

47. Wang, W.; Banerjee, S.; Jia, S.; Steigerwald, M. L.; Herman, I. P. Ligand Control of Growth, Morphology, and Capping Structure of Colloidal CdSe Nanorods. *Chem. Mater.* **2007**, *19*, 2573–2580.

48. Saunders, A. E.; Ghezelbash, A.; Sood, P.; Korgel, B. A. Synthesis of High Aspect Ratio Quantum-Size CdS Nanorods and Their Surface-Dependent Photoluminescence. *Langmuir* **2008**, *24*, 9043–9049.

49. Okamoto, K.; Kawai, S. Electrical Conduction and Phase Transition of Copper Sulfides. *Jpn. J. Appl. Phys.* **1973**, *12*.

50. Willets, K. A.; Van Duyne, R. P. Localized Surface Plasmon Resonance Spectroscopy and Sensing. *Annu. Rev. Phys. Chem.* **2007**, *58*, 267–297.

51. Flatau, P. J.; Draine, B. T. Fast Near Field Calculations in the Discrete Dipole Approximation for Regular Rectilinear Grids. *Opt. Express* **2012**, *20*, 1247–1252.

52. Draine, B. T.; Flatau, P. J. Discrete-Dipole Approximation for Scattering Calculations. *J. Opt. Soc. Am. A* **1994**, *11*, 1491–1499.

53. The DDA code was taken from the open source at <http://www.astro.princeton.edu/~draine/DDSCAT.html> (accessed December 2012).

54. Draine, B. T.; Flatau, P. J. User Guide for the Discrete Dipole Approximation Code DDSCAT 7.2. <http://arXiv.org/abs/1202.3424> (accessed December 2012).